
Graph Flow Matching: Enhancing Image Generation with Neighbor-Aware Flow Fields

Md Shahriar Rahim Siddiqui
 The University of British Columbia
 Vancouver, Canada
 shahriar.siddiqui@ubc.ca

Moshe Eliasof
 The University of Cambridge
 Cambridge, United Kingdom
 me532@cam.ac.uk

Eldad Haber
 The University of British Columbia
 Vancouver, Canada
 ehaber@eoas.ubc.ca

Abstract

Flow matching casts sample generation as learning a continuous-time velocity field that transports noise to data. Existing flow matching networks typically predict each point’s velocity independently, considering only its location and time along its flow trajectory, and ignoring neighboring points. However, this pointwise approach may overlook correlations between points along the generation trajectory that could enhance velocity predictions, thereby improving downstream generation quality. To address this, we propose Graph Flow Matching (GFM), a lightweight enhancement that decomposes the learned velocity into a reaction term—any standard flow matching network—and a diffusion term that aggregates neighbor information via a graph neural module. This reaction–diffusion formulation retains the scalability of deep flow models while enriching velocity predictions with local context, all at minimal additional computational cost. Operating in the latent space of a pretrained variational autoencoder, GFM consistently improves Fréchet Inception Distance (FID) and recall across five image generation benchmarks (LSUN Church, LSUN Bedroom, FFHQ, AFHQ-Cat, and CelebA-HQ at 256×256), demonstrating its effectiveness as a modular enhancement to existing flow matching architectures.

1 Introduction

Flow matching has recently gained traction as a promising generative modeling paradigm, framing sample synthesis as the integration of a learned (interpolated) continuous-time velocity field that deterministically or stochastically transforms noise into data [1, 2]. Given two distributions π_0 and π_1 , the task is to learn a velocity field $v(\mathbf{x}, t)$ that, when integrated, solves:

$$\dot{\mathbf{x}} = v(\mathbf{x}, t), \quad \mathbf{x}(0) \sim \pi_0, \quad \mathbf{x}(1) \sim \pi_1. \quad (1)$$

While highly effective, current flow matching architectures predict each point’s velocity *independently*, conditioning only on its (\mathbf{x}, t) coordinates without considering neighboring points. This overlooks a fundamental property of high-dimensional data: *local coherence*, where nearby points typically exhibit similar behaviors and follow in similar trajectories.

We propose **Graph Flow Matching (GFM)**, which enhances standard flow networks with neighbor awareness through a reaction-diffusion decomposition:

$$v(\mathbf{x}, t) = v_{\text{react}}(\mathbf{x}, t) + v_{\text{diff}}(\mathbf{x}, t; \mathcal{N}(\mathbf{x}, t)), \quad (2)$$

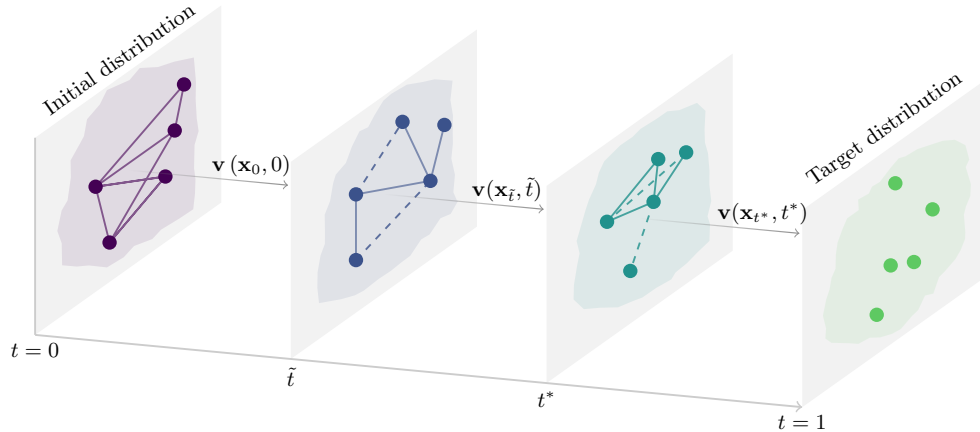


Figure 1: Graph flow matching enriches the flow trajectory from the initial distribution ($t = 0$) to the target distribution ($t = 1$) by incorporating neighborhood information at intermediate time steps. Graphs at each step—constructed via attention—guide local interactions; dashed edges indicate weaker influences.

where v_{react} is any standard flow network, and v_{diff} is a lightweight graph-based correction term that aggregates information from neighboring samples $\mathcal{N}(\mathbf{x}, t)$. Figure 1 illustrates this process, where the flow trajectory from π_0 to π_1 is augmented by incorporating neighborhood structure via graphs at intermediate time steps. Designing a flow matching pipeline requires two key decisions: *network architecture* and *training strategy* (e.g., Rectified Flow [3], Consistency FM [4]). We focus on the *architecture* aspect, proposing an enhancement compatible with any training objective and existing base flow network - pretrained or otherwise.

In this work, we adopt the latent-space generative modeling paradigm, popularized by work such as Stable Diffusion [5], and recently used for flow matching as in LFM [6], where image generation is performed in a perceptually compressed latent space produced by a pretrained variational autoencoder (VAE) [7]. This choice reduces computational cost as the latent space defines meaningful distance metrics for constructing graphs, which are easy to compute. Our contributions therefore operate entirely within this latent framework. Figures 2–3 qualitatively demonstrate our method’s effectiveness across three diverse datasets. Quantitatively, we validate GFM on five unconditional image generation benchmarks—LSUN Church [8], LSUN Bedroom [8], FFHQ [9], AFHQ-Cat [10], and CelebA-HQ [11] at 256×256 resolution, showing consistent improvements in Fréchet Inception Distance (FID) and recall while adding minimal computational overhead ($\lesssim 10\%$ additional parameters).

Our Contributions (i) We introduce Graph Flow Matching (GFM), a modular reaction–diffusion framework that enhances flow networks with neighbor-aware velocity correction. GFM decomposes the velocity field into a standard pointwise term (using any existing flow network) and a graph-based diffusion term, integrating seamlessly with existing backbones and training strategies without requiring modifications to losses or solvers; (ii) We validate GFM in the latent space of a pretrained VAE, demonstrating consistent improvements in unconditional image generation across five standard benchmarks, establishing our approach as a practical enhancement to existing flow matching architectures.

2 Background and Related Work

A central challenge in generative modeling is transporting a simple base distribution (e.g., Gaussian noise) into a complex, high-dimensional target distribution. This underpins models such as generative adversarial networks (GANs) [13], variational autoencoders (VAEs) [7], normalizing flows [14], and diffusion models [15, 16, 17]. Recent trends increasingly adopt continuous-time formulations. Continuous normalizing flows (CNFs) [2] generalize discrete flows by learning transformations via ODEs. Diffusion models, originally discrete-time [17], have evolved into continuous-time score-based models defined through stochastic differential equations (SDEs) [16]. Flow matching [1] offers



Figure 2: **Neighbor-aware flow matching enhances image generation.** FFHQ samples (256×256) generated using the same random seed by: **(top)** baseline ADM U-Net [6], **(middle)** ADM with MPNN-based correction, and **(bottom)** ADM with a GPS-based correction module [12]. GFM variants produce more coherent facial features and sharper details compared to the baseline model.

a deterministic, continuous-time alternative that avoids score estimation by directly supervising a velocity field that transports noise to data. It combines fast sampling and simplified training, making it an attractive framework for generative modeling. Our work builds upon this foundation by introducing a graph based architectural enhancement that enriches velocity predictions with information from neighboring points along the flow trajectory.

2.1 Flow Matching Preliminaries

Flow matching formulates sample generation as solving an ordinary differential equation (ODE) that transports a source distribution π_0 to a target distribution π_1 over a finite time horizon $t \in [0, 1]$. Given two random variables $X_0 \sim \pi_0$ and $X_1 \sim \pi_1$ with support in $\mathcal{X} \subseteq \mathbb{R}^d$, the goal is to learn a velocity field $v_\theta : \mathbb{R}^d \times [0, 1] \rightarrow \mathbb{R}^d$ such that the solution $\mathbf{x}(t)$ to the initial value problem

$$\dot{\mathbf{x}} = v_\theta(\mathbf{x}, t), \quad \mathbf{x}(0) \sim \pi_0, \quad (3)$$

satisfies $\mathbf{x}(1) \sim \pi_1$. Learning the velocity field from data fundamentally constitutes an interpolation problem over the joint domain $\mathcal{X} \times [0, 1]$. Given velocity supervision at a finite set of spatiotemporal points (\mathbf{x}_{t_i}, t_i) , the model must generalize to unseen points throughout this domain. Flow matching methods create synthetic supervision by sampling pairs $(\mathbf{x}_0, \mathbf{x}_1) \sim (\pi_0, \pi_1)$, selecting an interpolation time $t \in [0, 1]$, constructing an interpolation point \mathbf{x}_t between \mathbf{x}_0 and \mathbf{x}_1 , and defining a target velocity $\mathbf{v}^*(\mathbf{x}_t, t)$ according to a transport plan. For example, under constant-velocity transport:

$$\mathbf{v}^*(\mathbf{x}_t, t) = \mathbf{x}_1 - \mathbf{x}_0, \quad \mathbf{x}_t = (1 - t)\mathbf{x}_0 + t\mathbf{x}_1. \quad (4)$$

The training objective minimizes the squared error between predicted and target velocities:

$$\mathcal{L}_{\text{FM}}(\theta) = \mathbb{E}_{t, \mathbf{x}_0, \mathbf{x}_1} \left[\|v_\theta(\mathbf{x}_t, t) - \mathbf{v}^*(\mathbf{x}_t, t)\|^2 \right]. \quad (5)$$

This approach transforms sample generation into a supervised learning problem over velocity samples $(\mathbf{x}_t, t, \mathbf{v}^*)$ drawn from the joint space $\mathcal{X} \times [0, 1]$. At inference time, one generates new samples by numerically solving the learned ODE Equation 3 starting from $X_0 \sim \pi_0$.

2.2 Limitations of Pointwise Velocity Prediction

Current flow matching architectures predominantly adopt a pointwise prediction paradigm, directly regressing from query coordinates (\mathbf{x}_t, t) to velocity $v(\mathbf{x}_t, t)$ while treating each point as an independent interpolation task. This mirrors the limitation of early point cloud architectures like

PointNet [18], which process points independently to interpolate features and thus may struggle to model local geometric relationships, a constraint that PointNet++ [19] directly addressed by introducing hierarchical neighborhood aggregation. Similarly, methods like DGCNN [20] introduced dynamic graph construction, showing that explicitly modeling local neighborhood structure improves performance over purely pointwise processing.

Without such neighborhood awareness, pointwise methods may struggle in regions with sharp transitions, sparse supervision, or multiple modes [21, 22], and pointwise interpolation may fail to recover the underlying transport dynamics, leading to artifacts or degraded sample quality.

The core issue stems from overlooking a crucial inductive bias: *local coherence* [23]. In high-dimensional manifolds, points that are spatially proximate often belong to the same semantic region and follow similar trajectories [24, 25]. Just as nearby points in classification tasks tend to share labels, neighboring interpolation points in flow matching—particularly those along a shared trajectory—typically exhibit similar velocities. Neglecting this correlation structure may limit generalization, especially in regions of high curvature or sparse sampling where models must interpolate with limited local support [26].

2.3 Graph-based Approaches in Deep Learning

The limitations of pointwise processing have motivated significant research into graph-based architectures that explicitly model relationships between data points. Graph Neural Networks (GNNs) have emerged as a powerful framework for incorporating local structure, enabling each point to aggregate information from its neighbors through message passing mechanisms [27, 28].

In geometric deep learning, Graph Convolutional Networks (GCNs) [27], Graph Attention Networks (GATs) [28], and Message Passing Neural Networks (MPNNs) [29] have demonstrated the value of neighborhood aggregation across diverse domains. These architectures naturally encode inductive biases about local structure, leading to improved generalization in tasks ranging from molecular property prediction to social network analysis.

Recent work has also explored the connection between GNNs and partial differential equations (PDEs). [30] showed that the dynamics of PDEs can be encoded into GNN architectures, with the implicit PDE structure greatly influencing their suitability for specific tasks. This PDE-GNN connection provides a principled framework for designing graph architectures that capture desired physical dynamics, which is a key inspiration for the **MPNN** graph correction module used in our experiments, as outlined in Section 4.

2.4 Physical Inspiration: Reaction-Diffusion Systems

Reaction-diffusion systems [31], which model how substances spread and interact in space, provide a natural framework for incorporating local interactions into flow matching. In these systems, the evolution of a quantity $u(\mathbf{x}, t)$ is governed by:

$$\frac{\partial u}{\partial t} = D\Delta u + R(u), \tag{6}$$

where $D\Delta u$ represents diffusion and $R(u)$ represents reaction (pointwise dynamics).

This decomposition inspires our approach: by treating the standard flow matching velocity network as a reaction term and adding a graph based diffusion term, we enable velocity predictions to adapt based on local flow patterns. In particular, the reaction-diffusion equation is known to generate complex patterns [31] that can explain many natural processes. Previous work has successfully utilized this equation in the context of GNNs [32, 33, 34] for solving graph related problems.

2.5 Latent-Space Generative Modeling

Generating high-resolution images directly in pixel space is computationally expensive and often burdens generative models with the need to reconstruct low-level details that are perceptually insignificant. Latent-space generative modeling mitigates this challenge by performing generation in a lower-dimensional, semantically meaningful space. This approach, popularized by models like Stable Diffusion [5], uses a two-stage process: a VAE first compresses images into latent representations, and a generative model then operates within this latent space to model data distributions.

Formally, given a pre-trained VAE with encoder $E : \mathcal{X} \rightarrow \mathcal{Z}$ and decoder $D : \mathcal{Z} \rightarrow \mathcal{X}$, latent-space generative modeling learns to transform a prior distribution (e.g., Gaussian noise) into the distribution of encoded data points in \mathcal{Z} . The decoder D then reconstructs image samples from this latent trajectory. This formulation provides several critical advantages:

- **Dimensionality Reduction.** Working in latent space reduces spatial resolution and channel complexity (e.g., from $256 \times 256 \times 3$ images to $32 \times 32 \times 4$ latent tensors), significantly lowering memory and compute requirements.
- **Semantic Compression.** The VAE, trained with perceptual and reconstruction losses, discards high-frequency noise and retains structurally and semantically relevant content. This reduces the burden on the generative model to learn low-level detail.
- **Decoupled Design.** Generation and reconstruction are modular: the VAE handles image fidelity, while the generative model focuses solely on learning distributional transformations in latent space.

Building on this design, the *Latent Flow Matching (LFM)* framework [6] extends flow matching to this perceptually aligned latent space. Rather than learning stochastic score-based dynamics as in diffusion models, LFM learns a deterministic velocity field that transports noise into encoded data samples by solving an ODE in latent space. This enables faster inference, fewer function evaluations, and simplified training compared to pixel-space diffusion.

For GFM to be effective, it must connect “neighboring” points to a graph. An embedded space is, therefore, natural to us as it defines a distance in latent space, which is easy to compute and is meaningful for complex data. Therefore, we build GFM directly on this latent space setting. We adopt the same VAE architecture as LFM—namely, the Stable Diffusion VAE—which maps 256×256 RGB images into $32 \times 32 \times 4$ latent tensors. We retain all components of the LFM pipeline, including the constant-velocity transport plan, flow matching loss, and ODE solver. Our contribution lies exclusively in augmenting the velocity field $v_\theta(\mathbf{z}, t)$ with a neighbor-aware graph based correction term. While there are many possible architectures for this part, here, we experimented with two architectures discussed below (Section 3).

3 Graph Flow Matching

We propose *Graph Flow Matching (GFM)*, a modular enhancement to flow matching networks that integrates local neighborhood structure through a lightweight graph module. GFM operates under a reaction–diffusion framework and is model-agnostic, where the velocity field is decomposed into a standard reaction term which could be any off-the-shelf pointwise acting flow network, and a graph-based message passing term (the so-called “diffusion” term that we propose).

3.1 Reaction–Diffusion Decomposition

Given interpolation triplets $(\mathbf{x}, t, \mathbf{v})$ constructed via a transport plan during the training phase, GFM predicts the velocity at each point as:

$$v_\theta(\mathbf{x}, t) = v_{\text{react}}(\mathbf{x}, t) + v_{\text{diff}}(\mathbf{x}, t; \mathcal{N}(\mathbf{x}, t)), \quad (7)$$

where v_{react} is any off-the-shelf flow matching architecture, and v_{diff} is a graph-based correction term informed by a neighborhood $\mathcal{N}(\mathbf{x}, t)$ of surrounding samples at time t .

Graph Generation. In our formulation, each image represents a node on a graph, we therefore compute the graph connectivity using an attention mechanism applied to the latent representations of the images.

Reaction Term: Standard Flow Networks. The reaction term $v_{\text{react}}(\mathbf{x}, t)$ can be any off-the-shelf flow matching network that predicts velocity from spatial and temporal coordinates. It typically takes the form of a U-Net [35, 36], Vision Transformer [37, 38], or any pointwise neural interpolator. This component models pointwise transport based on global training dynamics.

In our experiments (Sec. 4), we instantiate v_{react} with a UNet (ADM) [36] and a transformer model (DiT) [38], following the settings in [6]. However, GFM is compatible with any flow matching backbone and training strategy.



Figure 3: LSUN Bedroom and LSUN Church samples (256×256) generated using the same random seed by: **(top)** baseline DiT-L/2 [6], **(middle)** DiT-L/2 with MPNN-based correction, and **(bottom)** DiT-L/2 with GPS-based graph correction [12]. GFM variants generate more complete spatial structures and sharper boundaries compared to the baseline model.

Diffusion Term: Neighbor-Aware Velocity Correction. While the diffusion term $v_{\text{diff}}(\mathbf{x}, t; \mathcal{N}(\mathbf{x}, t))$ can be implemented using any graph-based neural architecture that aggregates information from neighboring samples, here we focus on two such architectures: the Message Passing Neural Network (MPNN) [29] and a graph transformer architecture (GPS) [12].

MPNN Architecture. The first diffusion term we used is a custom MPNN architecture where we use a graph gradient \mathbf{G} (sometimes referred to as an incidence matrix) [30] to compute the difference between node features. This yields an edge-based quantity, or edge features. We then apply a nonlinearity to the edge features and aggregate them back to the node using the transpose of the incidence matrix. We then apply a non-linear network to the result. The network (Equation (7)) can thus be summarized by the following ODE

$$v_{\theta}(\mathbf{x}_t, t) = \frac{d\mathbf{x}_t}{dt} = -N_{\theta}^{(2)} \left(\mathbf{G}^{\top} \left[\sigma \left(\mathbf{G} N_{\theta}^{(1)}(\mathbf{x}_t, t) \right) \right], t \right) + R(\mathbf{x}_t, t), \quad (8)$$

where $R(\mathbf{x}_t, t)$ denotes the reaction term v_{react} , σ denotes a nonlinearity and $N_{\theta}^{(1)}$ and $N_{\theta}^{(2)}$ are lightweight convolutional networks. This network generalizes the classical MPNN that uses Multi-Layer Perceptrons (MLPs) for $N_{\theta}^{(1)}$ and $N_{\theta}^{(2)}$. While the node data for classical graphs is unstructured, in our experiments, each node in the graphs represents an image. Hence, we utilize convolutional architectures (such as UNets) for $N_{\theta}^{(1)}$ and $N_{\theta}^{(2)}$ in this paper.

GPS Architecture. Our second instantiation of the graph correction module employs the General, Powerful, Scalable (GPS) graph transformer architecture [12]. We adapt the GPS framework for flow matching as follows: (i) recasting each latent tensor in the batch as a node in a fully connected graph; (ii) integrating temporal information via learned time embeddings that are projected and concatenated with node features; (iii) incorporating random walk positional encodings (RWPE) generated at runtime using Pytorch Geometrics’s implementation; and (iv) replacing the standard GINEConv blocks with recurrent GatedGraphConv units. The GPS architecture alternates local message passing and global multi-head attention, allowing nodes to aggregate information from the entire batch. Finally, the network projects the enriched node representations back to the original latent tensor dimensions, producing the diffusion velocity correction term. The adjacency matrix of this setup is thus attention-based.

Below, we provide a lemma that theoretically reasons about the representational advantage of GFM compared with traditional pointwise flow networks. The proof can be found in the Appendix.

Table 1: Performance comparison on LSUN Church, FFHQ, and LSUN Bedroom datasets at 256×256 resolution. We report total parameters, diffusion term ($v_{\text{diff-net}}$) parameters, FID (lower is better), and recall (higher is better). Baseline parameter counts were computed from the checkpoints of [6] on our machine. Our results are highlighted in light blue. Corresponding FID ($True \rightarrow VAE$) values are: LSUN Church = 1.01, FFHQ = 1.05, LSUN Bedroom = 0.64.

Dataset/Model	Total Parameters (M)	$v_{\text{diff-net}}$ (M)	FID (\downarrow) VAE \rightarrow Flow	FID (\downarrow) True \rightarrow Flow	Recall (\uparrow)
LSUN Church					
ADM [6] (Baseline)	356.38	0	-	7.70	0.39
ADM+MPNN (Ours)	379.81	23.43	5.06	4.94	0.52
ADM+GPS (Ours)	374.20	18.13	4.67	4.61	0.51
DiT [6] (Baseline)	456.80	0	-	5.54	0.48
DiT+MPNN (Ours)	502.09	45.29	2.90	2.92	0.65
DiT+GPS (Ours)	481.25	24.45	2.89	3.10	0.66
FFHQ					
ADM [6] (Baseline)	406.40	0	-	8.07	0.40
ADM+MPNN (Ours)	429.82	23.43	5.61	5.90	0.62
ADM+GPS (Ours)	424.53	18.13	4.80	5.09	0.62
DiT [6] (Baseline)	456.80	0	-	4.55	0.48
DiT+MPNN (Ours)	480.23	23.43	3.80	4.52	0.66
DiT+GPS (Ours)	481.25	24.45	3.95	4.48	0.65
LSUN Bedroom					
ADM [6] (Baseline)	406.40	0	-	7.05	0.39
ADM+MPNN (Ours)	429.82	23.43	4.51	4.18	0.54
ADM+GPS (Ours)	424.53	18.13	4.26	3.97	0.56
DiT [6] (Baseline)	456.80	0	-	4.92	0.44
DiT+MPNN (Ours)	480.23	23.43	2.55	2.66	0.64
DiT+GPS (Ours)	481.25	24.45	3.31	3.57	0.65

Lemma 3.1 (Representational Advantage of Graph Flow Matching). *Let $\mathcal{L}_{FM}(v)$ be the flow matching loss for a velocity field v . The Graph Flow Matching model $v_{\theta}(\mathbf{x}, t) = v_{\text{react}}(\mathbf{x}, t) + v_{\text{diff}}(\mathbf{x}, t)$ achieves lower or equal training loss compared to the reaction-only model $v_{\text{react}}(\mathbf{x}, t)$ when both are trained to minimize the same objective:*

$$\mathcal{L}_{FM}(v_{\theta}) \leq \mathcal{L}_{FM}(v_{\text{react}}) \quad (9)$$

Furthermore, when the data exhibits local coherence, this inequality is strict.

Complexity. Graph Flow Matching (GFM) augments standard flow matching models with a diffusion term computed via a GNN, introducing an additional forward pass per ODE step. Each batch item corresponds to a node, yielding a graph with B nodes per step. The computational overhead depends on the graph topology: fully connected graphs scale as $\mathcal{O}(B^2)$ due to dense attention, while k -nearest neighbor (KNN) graphs scale as $\mathcal{O}(Bk)$ in both compute and memory. The reaction and diffusion terms are parameterized by separate networks, with the diffusion module adding only ~ 5 -10% to the total parameter count in our experiments. Importantly, GFM does not alter training objectives, solvers (e.g., Runge-Kutta, dopri5), or integration schedules. It preserves architectural compatibility while offering improved locality awareness at minimal additional cost.

4 Experiments

We evaluate Graph Flow Matching (GFM) on five standard unconditional image generation benchmarks: LSUN Church, LSUN Bedroom, FFHQ, AFHQ-Cat, and CelebA-HQ, all at 256×256 resolution. The goal is to assess the effect of incorporating neighbor-aware graph based correction into flow matching pipelines under consistent, state-of-the-art settings. We have added an additional ablation study in the Appendix.

Experimental Settings. To isolate the effect of the graph correction term, we retain all architecture and training settings from the latent flow matching (LFM) models of [6]. We therefore perform our

Table 2: Performance comparison on AFHQ-Cat and CelebA-HQ datasets at 256×256 resolution, computed entirely on our machine, with v_{react} architectures ADM and DiT-L/2 being taken from [6]. We report the total parameters, diffusion term ($v_{\text{diff-net}}$) parameters, FID scores (lower is better), and recall (higher is better). Our results are highlighted in light blue. Corresponding $FID(\text{True} \rightarrow \text{VAE})$ for the datasets are: AFHQ-Cat= 3.18, CelebA-HQ= 1.29

Dataset/Model	Total Parameters (M)	$v_{\text{diff-net}}$ (M)	FID (\downarrow) VAE \rightarrow Flow	FID (\downarrow) True \rightarrow Flow	Recall (\uparrow)
AFHQ-Cat					
ADM (Baseline)	153.10	0	7.40	7.34	0.32
ADM+MPNN	163.17	10.07	7.01	6.97	0.35
ADM+GPS	171.23	18.13	2.92	4.63	0.54
DiT (Baseline)	456.80	0	8.24	9.05	0.42
DiT+MPNN	480.23	23.43	7.19	8.07	0.51
DiT+GPS	481.25	24.45	8.21	8.98	0.42
CelebA-HQ					
ADM (Baseline)	153.10	0	7.54	6.80	0.50
ADM+MPNN	176.53	23.43	5.33	6.28	0.56
ADM+GPS	177.55	24.45	5.89	6.71	0.52
DiT (Baseline)	456.80	0	6.85	6.23	0.55
DiT+MPNN	480.49	23.43	5.85	6.16	0.57
DiT+GPS	481.25	24.45	6.09	6.18	0.59

experiments in the latent space of the pretrained VAE used by the aforementioned authors. Specifically, (i) **Backbones:** The $v_{\text{react}}(\mathbf{x}_t, t)$ terms we use are the ADM U-Net [36] and DiT Transformer [38] (specifically, the ADM variants and DiT-L/2 variant from [6]), representing leading convolutional and attention-based flow architectures; (ii) **Latent space:** The Stable Diffusion VAE [5], which maps 256×256 RGB images into $32 \times 32 \times 4$ latent tensors. All models operate exclusively in this latent space.¹; (iii) **Training strategy:** Constant-velocity flow matching loss (Equation (5)), the Dormand–Prince (dopri5) ODE integrator with $rtol = atol = 10^{-5}$, and unmodified training hyperparameters from LFM [6].

This ensures that any performance gain arises from our graph-based diffusion term (i.e., the graph correction module v_{diff}) rather than hyperparameter tuning or architectural shifts. We evaluate the two implementations of v_{diff} discussed in Section 3. The *MPNN* implementation uses neural components $N_{\theta}^{(1)}$ and $N_{\theta}^{(2)}$, for which we employ identical U-Net [35] architectures derived from the U-Net design of [39]. The *GPS* implementation, like MPNN, implements attention-based adjacency. Full architectural and hyperparameter details are provided in the Appendix.

To provide a nuanced assessment of generation quality, we introduce three FID metrics: (i) $FID(\text{True} \rightarrow \text{Flow})$, the standard FID computed between real and generated images; (ii) $FID(\text{True} \rightarrow \text{VAE})$, which measures the FID between real images and their reconstructions via the pretrained VAE (reported in table captions) to quantify reconstruction fidelity; and (iii) $FID(\text{VAE} \rightarrow \text{Flow})$, which compares VAE reconstructions with generated samples. These metrics allow us to distinguish generative fidelity from the limitations of the VAE encoder-decoder pipeline and to better interpret results within the latent space modeling framework.

Tables 1 and 2 report Fréchet Inception Distance (FID), recall, and parameter counts. Across all datasets and backbones, GFM consistently improves sample quality, achieving FID reductions of up to and sometimes exceeding 40% relative to the base models. These improvements are achieved with only modest computational overhead—typically less than a 10% increase in total parameters.

Qualitatively, GFM-enhanced models generate better-structured furniture and spatial layouts on LSUN Bedroom, sharper and more anatomically plausible faces on FFHQ, and more coherent architectural forms on LSUN Church as shown in Figures 2–3. The effectiveness of GFM across both convolutional (ADM) and transformer-based (DiT) models underscores its architectural generality.

¹The specific pretrained VAE used by [6]: <https://huggingface.co/stabilityai/sd-vae-ft-mse>

Table 3: Ablation study on graph structure in LSUN Church, FFHQ, and AFHQ-Cat datasets. We compare our graph-based diffusion term with the self-only diffusion baseline where the graph adjacency matrix is set to identity (Adj=I). FID scores and recall show that the graph structure improves performance.

Dataset/Model	Total Parameters (M)	$v_{\text{diff-net}}$ (M)	FID (\downarrow) VAE \rightarrow Flow	FID (\downarrow) True \rightarrow Flow	Recall (\uparrow)
LSUN Church					
ADM+GPS	374.20	18.13	4.67	4.61	0.51
ADM+GPS (Adj=I)	374.20	18.13	6.24	5.71	0.51
DiT+GPS	481.25	24.45	2.89	3.10	0.66
DiT+GPS (Adj=I)	481.25	24.45	4.63	4.80	0.64
FFHQ					
ADM+GPS	424.53	18.13	4.80	5.09	0.62
ADM+GPS (Adj=I)	424.53	18.13	6.12	6.58	0.59
DiT+GPS	481.25	24.45	3.95	4.48	0.65
DiT+GPS (Adj=I)	481.25	24.45	4.02	4.53	0.64
AFHQ-Cat					
ADM+GPS	171.23	18.13	2.92	4.63	0.54
ADM+GPS (Adj=I)	171.23	18.13	7.51	7.20	0.35
DiT+GPS	481.25	24.45	8.21	8.98	0.42
DiT+GPS (Adj=I)	481.25	24.45	8.26	9.01	0.41

To further assess the role of graph structure, we conduct an ablation in which the adjacency matrix of the GPS module is replaced with the identity matrix, thereby eliminating inter-node communication while preserving architectural and parameter parity. Note that for the MPNN module, setting the adjacency matrix to identity would lead to a zero gradient matrix \mathbf{G} . This would effectively cancel out the diffusion term, leaving only the reaction term v_{react} , making the MPNN architecture unsuitable for this particular ablation study. This ablation reduces GPS to a non-graph network and thus isolates the effect of the graph on the addition of a second network. Results in Table 3 show a clear degradation in FID and recall when graph connectivity is removed, confirming that performance gains stem from graph structure rather than parameter count or the addition of a second network alone. Notably, GFM provides consistent performance gains across both convolutional (ADM) and transformer-based (DiT) architectures. This underscores the generality of GFM as an architectural enhancement that is agnostic to the flow matching backbone v_{react} .

5 Conclusion

We introduced Graph Flow Matching (GFM), a lightweight architectural enhancement that improves the expressiveness of flow matching generative models by incorporating local neighborhood structure via a graph-based “diffusion” term. Through a reaction–diffusion decomposition, GFM enables pointwise velocity predictors to aggregate contextual information from neighboring samples along the flow trajectory—offering a principled and scalable mechanism for improving the interpolation of the flow field.

Our results demonstrate that GFM consistently enhances generative quality across multiple datasets and architectures, reducing FID and increasing recall with minimal computational overhead. Importantly, these improvements hold across both convolutional and transformer-based backbones, highlighting the generality of our approach.

Ablation studies confirm that performance gains arise from incorporating a graph, rather than merely from the addition of parameters or a second network. These findings underscore a broader principle: local correlations along the flow trajectory can be leveraged to improve sample quality.

Looking forward, we believe GFM opens several avenues for exploration and extensions to conditional or multimodal generation. More broadly, our work suggests that combining continuous-time genera-

tive frameworks with discrete geometric priors offers a promising direction for robust, high-fidelity generative modeling.

References

- [1] Yaron Lipman, Ricky T. Q. Chen, Heli Ben-Hamu, Maximilian Nickel, and Matt Le. Flow matching for generative modeling, 2023.
- [2] Ricky TQ Chen, Yulia Rubanova, Jesse Bettencourt, and David K Duvenaud. Neural ordinary differential equations. *Advances in neural information processing systems*, 31, 2018.
- [3] Xingchao Liu, Chengyue Gong, and Qiang Liu. Flow straight and fast: Learning to generate and transfer data with rectified flow. *arXiv preprint arXiv:2209.03003*, 2022.
- [4] Ling Yang, Zixiang Zhang, Zhilong Zhang, Xingchao Liu, Minkai Xu, Wentao Zhang, Chenlin Meng, Stefano Ermon, and Bin Cui. Consistency flow matching: Defining straight flows with velocity consistency. *arXiv preprint arXiv:2407.02398*, 2024.
- [5] Robin Rombach, Andreas Blattmann, Dominik Lorenz, Patrick Esser, and Björn Ommer. High-resolution image synthesis with latent diffusion models. In *Proceedings of the IEEE/CVF conference on computer vision and pattern recognition*, pages 10684–10695, 2022.
- [6] Quan Dao, Hao Phung, Binh Nguyen, and Anh Tran. Flow matching in latent space. *arXiv preprint arXiv:2307.08698*, 2023.
- [7] Diederik P Kingma and Max Welling. Auto-encoding variational bayes, 2022.
- [8] Fisher Yu, Yinda Zhang, Shuran Song, Ari Seff, and Jianxiong Xiao. Lsun: Construction of a large-scale image dataset using deep learning with humans in the loop. *arXiv preprint arXiv:1506.03365*, 2015.
- [9] Tero Karras, Samuli Laine, and Timo Aila. A style-based generator architecture for generative adversarial networks. In *Proceedings of the IEEE/CVF conference on computer vision and pattern recognition*, pages 4401–4410, 2019.
- [10] Yunjey Choi, Youngjung Uh, Jaejun Yoo, and Jung-Woo Ha. Stargan v2: Diverse image synthesis for multiple domains. In *Proceedings of the IEEE Conference on Computer Vision and Pattern Recognition*, 2020.
- [11] Tero Karras, Timo Aila, Samuli Laine, and Jaakko Lehtinen. Progressive growing of gans for improved quality, stability, and variation. In *International Conference on Learning Representations*, 2018.
- [12] Ladislav Rampášek, Michael Galkin, Vijay Prakash Dwivedi, Anh Tuan Luu, Guy Wolf, and Dominique Beaini. Recipe for a general, powerful, scalable graph transformer. *Advances in Neural Information Processing Systems*, 35:14501–14515, 2022.
- [13] Ian J Goodfellow, Jean Pouget-Abadie, Mehdi Mirza, Bing Xu, David Warde-Farley, Sherjil Ozair, Aaron Courville, and Yoshua Bengio. Generative adversarial nets. *Advances in neural information processing systems*, 27, 2014.
- [14] George Papamakarios, Eric Nalisnick, Danilo Jimenez Rezende, Shakir Mohamed, and Balaji Lakshminarayanan. Normalizing flows for probabilistic modeling and inference. *Journal of Machine Learning Research*, 22(57):1–64, 2021.
- [15] Yang Song and Stefano Ermon. Generative modeling by estimating gradients of the data distribution. *Advances in neural information processing systems*, 32, 2019.
- [16] Yang Song, Jascha Sohl-Dickstein, Diederik P. Kingma, Abhishek Kumar, Stefano Ermon, and Ben Poole. Score-based generative modeling through stochastic differential equations, 2021.
- [17] Jonathan Ho, Ajay Jain, and Pieter Abbeel. Denoising diffusion probabilistic models. *Advances in neural information processing systems*, 33:6840–6851, 2020.

- [18] Charles R Qi, Hao Su, Kaichun Mo, and Leonidas J Guibas. Pointnet: Deep learning on point sets for 3d classification and segmentation. In *Proceedings of the IEEE Conference on Computer Vision and Pattern Recognition*, pages 652–660, 2017.
- [19] Charles R Qi, Li Yi, Hao Su, and Leonidas J Guibas. Pointnet++: Deep hierarchical feature learning on point sets in a metric space. *arXiv preprint arXiv:1706.02413*, 2017.
- [20] Yue Wang, Yongbin Sun, Ziwei Liu, Sanjay E. Sarma, Michael M. Bronstein, and Justin M. Solomon. Dynamic graph cnn for learning on point clouds. *ACM Trans. Graph.*, 38(5), October 2019.
- [21] Phil Pope, Chen Zhu, Ahmed Abdelkader, Micah Goldblum, and Tom Goldstein. The intrinsic dimension of images and its impact on learning. In *International Conference on Learning Representations*.
- [22] Binxu Wang and Carlos R Ponce. A geometric analysis of deep generative image models and its applications. In *International Conference on Learning Representations*.
- [23] Bei Wang, Brian Summa, Valerio Pascucci, and Mikael Vejdemo-Johansson. Branching and circular features in high dimensional data. *IEEE Transactions on Visualization and Computer Graphics*, 17(12):1902–1911, 2011.
- [24] D. Mu noz, O. Allix, F. Chinesta, J.J. Ródenas, and E. Nadal. Manifold learning for coherent design interpolation based on geometrical and topological descriptors. *Computer Methods in Applied Mechanics and Engineering*, 405:115859, 2023.
- [25] Ruonan Zhang, Jingyi Chen, Wei Gao, Ge Li, and Thomas H. Li. Pointot: Interpretable geometry-inspired point cloud generative model via optimal transport. *IEEE Transactions on Circuits and Systems for Video Technology*, 32(10):6792–6806, 2022.
- [26] Minhyeok Lee. The geometry of feature space in deep learning models: A holistic perspective and comprehensive review. *Mathematics*, 11(10), 2023.
- [27] Thomas N. Kipf and Max Welling. Semi-supervised classification with graph convolutional networks. In *International Conference on Learning Representations (ICLR)*, 2017.
- [28] Petar Veličković, Guillem Cucurull, Arantxa Casanova, Adriana Romero, Pietro Liò, and Yoshua Bengio. Graph Attention Networks. *International Conference on Learning Representations*, 2018. accepted as poster.
- [29] Justin Gilmer, Samuel S. Schoenholz, Patrick F. Riley, Oriol Vinyals, and George E. Dahl. Neural message passing for quantum chemistry. In Doina Precup and Yee Whye Teh, editors, *Proceedings of the 34th International Conference on Machine Learning*, volume 70 of *Proceedings of Machine Learning Research*, pages 1263–1272. PMLR, 06–11 Aug 2017.
- [30] Moshe Eliasof, Eldad Haber, and Eran Treister. Pde-gcn: Novel architectures for graph neural networks motivated by partial differential equations. In M. Ranzato, A. Beygelzimer, Y. Dauphin, P.S. Liang, and J. Wortman Vaughan, editors, *Advances in Neural Information Processing Systems*, volume 34, pages 3836–3849. Curran Associates, Inc., 2021.
- [31] Alan Mathison Turing. The chemical basis of morphogenesis. *Bulletin of mathematical biology*, 52:153–197, 1990.
- [32] Eldad Haber, Keegan Lensink, Eran Treister, and Lars Ruthotto. Imexnet a forward stable deep neural network. In *International Conference on Machine Learning*, pages 2525–2534. PMLR, 2019.
- [33] Jeongwhan Choi, Seoyoung Hong, Noseong Park, and Sung-Bae Cho. Gread: Graph neural reaction-diffusion networks. In *International Conference on Machine Learning*, pages 5722–5747. PMLR, 2023.
- [34] Moshe Eliasof, Eldad Haber, and Eran Treister. Graph neural reaction diffusion models. *SIAM Journal on Scientific Computing*, 46(4):C399–C420, 2024.

- [35] Olaf Ronneberger, Philipp Fischer, and Thomas Brox. U-net: Convolutional networks for biomedical image segmentation. In *Medical image computing and computer-assisted intervention—MICCAI 2015: 18th international conference, Munich, Germany, October 5-9, 2015, proceedings, part III 18*, pages 234–241. Springer, 2015.
- [36] Prafulla Dhariwal and Alexander Nichol. Diffusion models beat gans on image synthesis. In M. Ranzato, A. Beygelzimer, Y. Dauphin, P.S. Liang, and J. Wortman Vaughan, editors, *Advances in Neural Information Processing Systems*, volume 34, pages 8780–8794. Curran Associates, Inc., 2021.
- [37] Alexey Dosovitskiy, Lucas Beyer, Alexander Kolesnikov, Dirk Weissenborn, Xiaohua Zhai, Thomas Unterthiner, Mostafa Dehghani, Matthias Minderer, Georg Heigold, Sylvain Gelly, et al. An image is worth 16x16 words: Transformers for image recognition at scale. *arXiv preprint arXiv:2010.11929*, 2020.
- [38] William Peebles and Saining Xie. Scalable diffusion models with transformers. In *Proceedings of the IEEE/CVF international conference on computer vision*, pages 4195–4205, 2023.
- [39] Chin-Wei Huang, Jae Hyun Lim, and Aaron C Courville. A variational perspective on diffusion-based generative models and score matching. *Advances in Neural Information Processing Systems*, 34:22863–22876, 2021.
- [40] Arash Vahdat, Karsten Kreis, and Jan Kautz. Score-based generative modeling in latent space. *Advances in neural information processing systems*, 34:11287–11302, 2021.
- [41] Hao Phung, Quan Dao, and Anh Tran. Wavelet diffusion models are fast and scalable image generators. In *Proceedings of the IEEE/CVF conference on computer vision and pattern recognition*, pages 10199–10208, 2023.
- [42] Zhisheng Xiao, Karsten Kreis, and Arash Vahdat. Tackling the generative learning trilemma with denoising diffusion gans. In *International Conference on Learning Representations*.
- [43] Yang Song, Jascha Sohl-Dickstein, Diederik P Kingma, Abhishek Kumar, Stefano Ermon, and Ben Poole. Score-based generative modeling through stochastic differential equations. In *International Conference on Learning Representations*, 2021.
- [44] Tero Karras, Miika Aittala, Janne Hellsten, Samuli Laine, Jaakko Lehtinen, and Timo Aila. Training generative adversarial networks with limited data. *Advances in neural information processing systems*, 33:12104–12114, 2020.
- [45] Ségolène Tiffany Martin, Anne Gagneux, Paul Hagemann, and Gabriele Steidl. Pnp-flow: Plug-and-play image restoration with flow matching. In *The Thirteenth International Conference on Learning Representations*, 2025.
- [46] Kurt Hornik, Maxwell Stinchcombe, and Halbert White. Multilayer feedforward networks are universal approximators. *Neural networks*, 2(5):359–366, 1989.
- [47] Eero P Simoncelli and Bruno A Olshausen. Natural image statistics and neural representation. *Annual review of neuroscience*, 24(1):1193–1216, 2001.
- [48] Michael M Bronstein, Joan Bruna, Yann LeCun, Arthur Szlam, and Pierre Vandergheynst. Geometric deep learning: going beyond euclidean data. *IEEE Signal Processing Magazine*, 34(4):18–42, 2017.
- [49] Michaël Defferrard, Xavier Bresson, and Pierre Vandergheynst. Convolutional neural networks on graphs with fast localized spectral filtering. *Advances in neural information processing systems*, 29, 2016.
- [50] Patrick Esser, Robin Rombach, Andreas Blattmann, and Bjorn Ommer. Imagebart: Bidirectional context with multinomial diffusion for autoregressive image synthesis. *Advances in neural information processing systems*, 34:3518–3532, 2021.
- [51] Axel Sauer, Kashyap Chitta, Jens Müller, and Andreas Geiger. Projected gans converge faster. *Advances in Neural Information Processing Systems*, 34:17480–17492, 2021.

- [52] Tero Karras, Timo Aila, Samuli Laine, and Jaakko Lehtinen. Progressive growing of gans for improved quality, stability, and variation. In *International Conference on Learning Representations*, 2018.
- [53] Zhendong Wang, Huangjie Zheng, Pengcheng He, Weizhu Chen, and Mingyuan Zhou. Diffusion-gan: Training gans with diffusion. In *The Eleventh International Conference on Learning Representations*.

A Appendix

This appendix provides supplementary material including implementation details, the theoretical justification for Lemma 3.1 and extended experimental results. We organize it into the following sections:

- Section B: Proof of Lemma 3.1
- Section C: Experimental details
- Section D: Diffusion-reaction with KNN ablation study
- Section E: Image generation timing analysis
- Section F: Comparison against leading generative models.
- Section G: Additional generated samples

B Proof of Lemma 3.1

Proof. The inequality follows from the function space representable by $v_\theta = v_{\text{react}} + v_{\text{diff}}$ strictly including the space representable by v_{react} alone [46]. At minimum, v_{diff} could learn to be zero, recovering v_{react} 's performance. For data with local coherence, where velocity varies smoothly across the manifold (common in natural images [47]), graph neural networks effectively exploit this structure [48, 49]. The graph diffusion term leverages local structure through message passing, allowing each point to aggregate information from its neighbors to better capture the local geometry of the flow. \square

This completes the proof that the inequality is strict when the data exhibits local coherence.

C Experimental Details

We implemented our code using PyTorch (offered under BSD-3 Clause license) and conducted experiments on Nvidia hardware (RTX 4090 for ADM UNet variants and RTX A6000 for DiT-L/2 experiments). All models from [6] were evaluated under identical conditions, with experiment tracking via Weights and Biases (wandb). The following subsections detail our datasets, architectures, and hyperparameter settings.

C.1 Datasets

We follow the exact preprocessing pipelines of [6] for all datasets, including VAE encoding at 256×256 resolution. To characterize the intrinsic variability of each dataset, we compute an internal FID score by randomly splitting each dataset into two non-overlapping halves and measuring the FID between them. Higher internal FID values indicate greater intrinsic variability within the dataset (Table 4).

Table 4: Internal FID scores across datasets, computed as the FID between two non-overlapping halves of each dataset. Higher values indicate greater intrinsic variability.

Dataset	Internal FID (\downarrow)
AFHQ-Cat	4.997
CelebA-HQ	2.014
FFHQ	1.123
LSUN Church	0.416
LSUN Bedroom	0.020

LSUN Church. The LSUN Church dataset [8] comprises approximately 126,227 training images of outdoor church buildings and architectural structures. This dataset presents particular challenges due to the complexity of architectural details and structural coherence required in the generated images.

LSUN Bedroom. The LSUN Bedroom dataset [8] contains around 3,033,042 training images of indoor bedroom scenes, making it substantially larger than the other datasets used in our experiments. This dataset features complex indoor environments with various furniture arrangements, lighting conditions, and textures, requiring models to capture both local details and global room layouts.

FFHQ. The Flickr-Faces-HQ (FFHQ) dataset [9] consists of 70,000 high-quality human portrait photographs. This dataset is particularly challenging for generative models as human faces contain subtle details that are easily perceived when incorrectly generated, making it an excellent benchmark for evaluating generative fidelity.

AFHQ-Cat. The AFHQ-Cat subset [10] contains $\sim 5,000$ training images of cat faces from the Animal Faces-HQ dataset. Despite its smaller size compared to the other datasets, it presents unique challenges in capturing fine details of animal features and fur textures.

CelebA-HQ. The CelebA-HQ dataset [11] provides 30,000 celebrity face images. This dataset is a high-quality version of the original CelebA dataset, with improved resolution and reduced compression artifacts. CelebA-HQ features greater diversity in facial attributes, expressions, and backgrounds compared to FFHQ, though with a stronger bias toward frontal-facing poses and celebrity appearances.

For all datasets, we evaluate our models using standard metrics computed over 50,000 generated samples. The generative models operate in the latent space of the VAE, with final images obtained by decoding the generated latents.

C.2 Training Algorithm

We train our latent flow matching models as in LFM ([6]), where the authors used the convention that noise is at $t = 1$ and the target distribution is at $t = 0$, which we summarize here. At each iteration, a real image x_0 from the data distribution p_0 is sampled and encoded into latent space via the VAE encoder E , yielding $z_0 = E(x_0)$. A sample from a standard Gaussian latent $z_1 \sim \mathcal{N}(0, I)$ is then taken and a single time $t \sim \mathcal{U}(0, 1)$ is drawn. The interpolation point $z_t = (1 - t)z_0 + tz_1$ lies along the straight-line transport plan between z_0 and z_1 . Then, the instantaneous velocity $v_\theta(z_t, t)$ is predicted with the flow network and the squared-error loss against the true transport increment $z_1 - z_0$ is computed. Finally, all network parameters are updated by gradient descent on this loss.

C.3 Network configurations

The network configurations for v_{react} for ADM from [6] are provided in Table 6 and that for DiT-L/2 can be found in [6] and in the corresponding GitHub repository.² Those for v_{diff} are provided in Table 5 and Table 7.

C.3.1 MPNN Diffusion Architecture

The MPNN diffusion module implements the velocity correction term v_{diff} using a message-passing neural network architecture inspired by the connection between graph neural networks and partial differential equations. As described in Equation (8), our MPNN architecture models the diffusion term as:

$$v_{\text{diff}}(\mathbf{x}_t, t) = -N_\theta^{(2)} \left(\mathbf{G}^\top \left[\sigma \left(\mathbf{G} N_\theta^{(1)}(\mathbf{x}_t, t) \right) \right], t \right),$$

where \mathbf{G} is the graph gradient operator that computes differences between connected node features, σ is a nonlinearity (we used the ELU function in all our experiments), and $N_\theta^{(1)}$ and $N_\theta^{(2)}$ are identical U-Net architectures (from [39], with code obtained from [45]) whose architectural hyperparameters are shown in Table 5. The graph gradient \mathbf{G} is constructed dynamically using attention-based adjacency, enabling the model to adapt its neighborhood structure based on the input latent representations.

²<https://github.com/VinAIRResearch/LFM/tree/main>

⁴Implementation adapted from <https://github.com/annegnx/PnP-Flow>

Table 5: Architectural hyperparameters for models using MPNN as the diffusion term (v_{diff}). Both $N_{\theta}^{(1)}$ and $N_{\theta}^{(2)}$ use identical U-Net architectures from [39]⁴ with the parameters shown.

Dataset	v_{react}	Base Channels	Channel Mult	Res Blocks	Attn. Resolutions
LSUN Church	ADM	85	[1, 2, 2]	2	(32, 16)
	DiT	85	[1, 2, 2]	5	(32, 16)
LSUN Bedroom	ADM	85	[1, 2, 2]	2	(32, 16)
	DiT	85	[1, 2, 2]	2	(32, 16)
FFHQ	ADM	85	[1, 2, 2]	2	(32, 16)
	DiT	85	[1, 2, 2]	2	(32, 16)
AFHQ-Cat	ADM	70	[1, 2]	2	(32, 16)
	DiT	85	[1, 2, 2]	2	(32, 16)
CelebA-HQ	ADM	85	[1, 2, 2]	2	(32, 16)
	DiT	85	[1, 2, 2]	2	(32, 16)

Table 6: ADM v_{react} configurations taken from [6]. The CelebA-HQ* configuration is the one obtained by testing the corresponding checkpoint from [6].

	FFHQ & Bed (256)	Church (256)	CelebA-HQ*
# ResNet blocks per scale	2	2	2
Base channels	256	256	256
Channel multiplier per scale	1,2,3,4	1,2,3,4	1,2,2,2
Attention resolutions	16,8,4	16,8	16,8
Channel multiplier for embeddings	4	4	4
Label dimensions	0	0	0

C.3.2 GPS Diffusion Architecture

The GPS diffusion module implements the velocity correction term v_{diff} using a graph transformer architecture as described in Section 3. We adapted the implementation from the PyTorch Geometric repository⁵. Table 7 presents the hyperparameters used for each dataset in our GPS module experiments. The module:

- Projects latent tensors into a fixed-width embedding space (Hidden Dim)
- Processes node features through multiple graph transformer layers (Layers)
- Captures graph structure using random walk positional encodings of specified dimension and length (PE Dim, Walk Length)
- Applies temporal conditioning via learnable sinusoidal embeddings (Time Channels)
- Integrates information across nodes using multi-head attention mechanisms

The architecture combines GatedGraphConv operations for local message passing with transformer-style attention for global interactions. Graph connectivity is computed dynamically at each step through learnable attention weights, enabling adaptive neighborhood formation between latent representations.

C.4 Training Hyperparameters

We evaluated GFM using two reaction term architectures: DiT-L/2 and ADM U-Net. For both, we initialized v_{react} with corresponding architectures and checkpoints from [6], then jointly trained the reaction and graph correction (“diffusion term”) components. For AFHQ-Cat experiments, we used the CelebA-HQ checkpoints to initialize the reaction terms. For evaluation of performance metrics, FID scores were monitored every 3K iterations, with training terminating after 80K iterations without

⁵https://github.com/pyg-team/pytorch_geometric/blob/master/examples/graph_gps.py

Table 7: Architectural hyperparameters for GPS-based diffusion term (v_{diff}). All models used multihead attention with 4 heads and time embeddings with 8 learnable frequencies.

Dataset	v_{react}	Hidden Dim	Layers	PE Dim	Walk Length	Time Channels
LSUN Church	ADM	256	16	16	20	64
	DiT	300	16	16	20	64
LSUN Bedroom	ADM	256	16	16	20	64
	DiT	300	16	16	20	64
FFHQ	ADM	256	16	16	20	64
	DiT	300	16	16	20	64
AFHQ-Cat	ADM	256	16	16	20	64
	DiT	300	16	16	20	64
CelebA-HQ	ADM	300	16	16	20	64
	DiT	300	16	16	20	64

Table 8: Training hyperparameters when v_{react} is DiT-L/2 across datasets. All models used AdamW optimizer with $\beta_1 = 0.9, \beta_2 = 0.999$.

v_{diff}	Parameter	LSUN Church	FFHQ	LSUN Bedroom	AFHQ-Cat	CelebA-HQ
MPNN	Learning rate	10^{-4}	$2 \cdot 10^{-4}$	10^{-4}	10^{-4}	$2 \cdot 10^{-4}$
	Batch size	42	32	32	20	32
	Training iter.	40K	40K	60K	60K	60K
	# GPUs	1	1	1	1	1
GPS	Learning rate	10^{-4}	$2 \cdot 10^{-4}$	10^{-4}	10^{-4}	$2 \cdot 10^{-4}$
	Batch size	32	32	32	32	32
	Training iter.	40K	40K	40K	60K	60K
	# GPUs	1	1	1	1	1

improvement. We saved models with the best FID scores and evaluated them using 50K generated samples. For CelebA-HQ comparisons, we obtained higher, i.e., worse FID scores than reported in [6] when evaluating their provided checkpoints on our machines⁶. To establish fair baselines, we trained these checkpoints for an additional 100K iterations using the training settings in [6] and used the models with the lowest FID scores as the baseline models for the corresponding DiT and ADM experiments.

Tables 8 and 9 detail the training hyperparameters for our GFM variants with DiT-L/2 and ADM U-Net backbones. All models used AdamW optimization with $\beta_1 = 0.9$ and $\beta_2 = 0.999$. The original training settings for the [6] checkpoints are provided in Tables 10 and 11. Similar to [6], a cosine annealing scheduler was used for the learning rate. For ablation studies in Table 3 with identity adjacency matrices, all other settings (besides their adjacency matrices) remained identical to their corresponding graph-based experiments.

D Ablation Study: Diffusion-Reaction with KNN

In this ablation, we swap out our attention-based adjacency for a simple k -nearest-neighbour (KNN) graph in latent space: for each node, we connect to its k closest latents and assign each edge a learnable weight, so that in the diffusion term, information is aggregated strictly from a node’s top- k neighbors instead of via attention scores. Concretely, we implement the diffusion term as a graph Laplacian multiplied by a per-channel diffusivity vector, mirroring the physical reaction–diffusion system in Equation (6). The overall velocity field remains the sum of the original flow-matching “reaction” network and this KNN-based “diffusion” operator. Let $X \in \mathbb{R}^{B \times C \times H \times W}$ be the batch of

⁶<https://github.com/VinAIRResearch/LFM/tree/main>

Table 9: Training hyperparameters when v_{react} is ADM [6] across datasets. All models used AdamW optimizer with $\beta_1 = 0.9, \beta_2 = 0.999$.

v_{diff}	Parameter	LSUN Church	FFHQ	LSUN Bedroom	AFHQ-Cat	CelebA-HQ
MPNN	Learning rate	$5 \cdot 10^{-5}$	$2 \cdot 10^{-5}$	$5 \cdot 10^{-5}$	$5 \cdot 10^{-5}$	10^{-4}
	Batch size	50	128	50	85	112
	Training iter.	50K	120K	40K	200K	60K
	# GPUs	1	1	1	1	1
GPS	Learning rate	$5 \cdot 10^{-5}$	$2 \cdot 10^{-5}$	$5 \cdot 10^{-5}$	$5 \cdot 10^{-5}$	10^{-4}
	Batch size	128	85	85	128	112
	Training iter.	50K	120K	40K	200K	60K
	# GPUs	1	1	1	1	1

Table 10: Training hyperparameters for the ADM checkpoints used as v_{react} , reproduced exactly from [6].

	CelebA 256	FFHQ	Church & Bed
lr	5e-5	2e-5	5e-5
Adam optimizer (β_1, β_2)	(0.9,0.999)	(0.9,0.999)	(0.9,0.999)
Batch size	112	128	128
# epochs	600	500	500
# GPUs	2	1	1
# training days	1.3	4.4	6.9 & 7.3

latent tensors at time t . This network implements:

$$\frac{dX}{dt}(t) = v_{\text{react}}(X(t), t) + \underbrace{\kappa_{\theta}(X(t), t)}_{\text{per-channel diffusivity}} \odot [L(X(t)) X_{\text{flat}}(t)], \quad (10)$$

where:

- $v_{\text{react}}(X, t)$ is a UNet variant from [39], with code taken from the GitHub repository of [45].
- $\kappa_{\theta}(X, t) \in \mathbb{R}^{B \times C}$ is a *per-example, per-channel* diffusivity vector produced by

$$Z = \text{UNet}(X, t), \quad \kappa_{\theta}(X, t) = \sigma(\text{GAP}(Z)),$$

where GAP is global average pooling to shape (B, C) and σ is a smooth activation (we used ELU in our experiments).

- $L(X) = I - D^{-1/2} A D^{-1/2}$ is the *normalized graph Laplacian* on the batch. We build the adjacency $A \in \mathbb{R}^{B \times B}$ by:
 1. Computing pairwise cosine similarities $\text{sim}_{ij} = \frac{X_i \cdot X_j}{\|X_i\| \|X_j\|}$.
 2. For each node i , selecting its top- K neighbors and assigning each neighbor rank $r \in \{0, \dots, K\}$ a learnable weight w_r .
 3. Masking to retain only these K edges, then row-normalizing so that each row of A sums to one.
- $X_{\text{flat}} \in \mathbb{R}^{B \times (C H W)}$ denotes each tensor flattened along spatial dimensions, and “ \odot ” broadcasts κ_{θ} across spatial axes.

Equation (10) thus decomposes the velocity into a standard flow-matching “reaction” term v_{react} and a KNN-based “diffusion” term given by the graph Laplacian $L(X)$ scaled per-channel by $\kappa_{\theta}(X, t)$. This KNN diffusion introduces local coupling across the batch at a cost of $\mathcal{O}(B K)$ per step.

To isolate the impact of graph structure from parameter count, we conducted a controlled ablation study on AFHQ-Cat using KNN-based graph diffusion. The architectural hyperparameters for the networks used are provided in Table 13. All models were trained for up to 2500 epochs with early-stopping, with a patience of 400 epochs and a learning rate of 10^{-4} . Table 12 presents these results,

Table 11: Training hyperparameters for the DiT checkpoints used as v_{react} , reproduced exactly from [6].

	CelebA 256	FFHQ	Church & Bed
Model	DiT-L/2	DiT-L/2	DiT-L/2
lr	2e-4	2e-4	1e-4
AdamW optimizer (β_1, β_2)	(0.9,0.999)	(0.9,0.999)	(0.9,0.999)
Batch size	32	32	96 & 32
# epochs	500	500	500
# GPUs	1	1	2 & 1
# training days	5.8	5.5	6.1 & 12.5

Table 12: Ablation study comparing KNN-based GFM variants against baseline models that use only the reaction term v_{react} on AFHQ-Cat at 256×256 resolution. Two baseline models (“noDiff”) are shown with different random seeds (0 and 100) to account for initialization variance. The baseline models contain 18.62M parameters, while GFM variants have 18.47M parameters. Samples were generated using Runge-Kutta (RK4) integration with 3 steps. Evaluation metrics are computed on 50,000 generated samples. Corresponding $FID(\text{True} \rightarrow \text{VAE})$ for AFHQ-Cat = 3.18.

Model	Batch	Total Parameters (M)	$v_{\text{diff-net}}$ (M)	FID (\downarrow) VAE \rightarrow Flow	FID (\downarrow) True \rightarrow Flow	KID (\downarrow)	Recall (\uparrow)
noDiff (seed = 0)	100	18.62	0	16.96	17.78	$1.37 \cdot 10^{-2}$	0.21
noDiff (seed = 100)	64	18.62	0	15.72	15.26	$1.17 \cdot 10^{-2}$	0.32
KNN ($k = 5$)	85	18.47	5.54	12.90	12.32	$8.07 \cdot 10^{-3}$	0.38
KNN ($k = 10$)	64	18.47	5.54	11.82	11.33	$7.65 \cdot 10^{-3}$	0.38
KNN ($k = 20$)	64	18.47	5.54	11.64	10.91	$6.94 \cdot 10^{-3}$	0.36

comparing GFM variants (with $k = 5, 10, 20$ neighbors) against baseline models without diffusion terms (“noDiff” in the table). Notably, we ensured the baseline models had slightly more parameters (18.62M vs. 18.47M) by increasing their width (number of channels), eliminating the possibility that improved performance stems merely from additional capacity. KNN-based GFM variants consistently outperform these wider baselines across all metrics, demonstrating that neighborhood structure rather than parameter count drives improvement.

E Timing of Image Generation

The ADM runs were conducted on an Nvidia RTX 4090 (24 GB) GPU and the DiT runs on an Nvidia A6000 (48 GB) GPU. We measured the time required for image generation in Table 14 using the Nvidia A6000 GPU for all models. The number of function evaluations (NFE) and times required to generate 1 image are reported. The corresponding timing results for the checkpoints from [6] were evaluated on our GPU.

As shown in Table 14, GFM models require approximately the same number of function evaluations as the baselines, with most variants showing statistically indistinguishable NFEs (confidence intervals overlap) or even slightly lower NFEs in some variants. The primary computational overhead comes from the additional graph processing, which increases sampling time. While there is a modest increase in wall-clock time, this also yields substantially improved performance as can be seen in the table. For example, DiT+MPNN achieves a 47% reduction in FID (from 5.54 to 2.92) on LSUN Church while maintaining comparable NFE, demonstrating that graph-based corrections significantly boost generation quality without additional solver steps and with minimal extra parameters (Table 1, Table 2).

⁸Implementation adapted from <https://github.com/annegnx/PnP-Flow>

Table 13: Architectural hyperparameters for the KNN-based diffusion term ablation study (Appendix D) whose results are presented in Table 12. All models use U-Net architectures from [39]⁸ and were trained for 2500 epochs with early stopping (patience=400 epochs).

Model	Component	Base Channels	Channel Mult	Res Blocks	Attn Resolutions
KNN ($k = 5, 10, 20$)	v_{react}	100	[1, 2]	3	(32, 16)
	κ_{θ} -net (v_{diff})	54	[1, 2]	5	(32, 16)
noDiff	v_{react} only	120	[1, 2]	3	(32, 16)

F Comparison with Leading Generative Models

Table 15 compares our GFM variants—ADM+MPNN, ADM+GPS, DiT+MPNN, and DiT+GPS—to a range of leading generative models, including deterministic flow matching (FM) [1], latent diffusion (LDM) [5], wavelet diffusion (WaveDiff) [41], DDPM [17], ImageBART [50], and top GANs (StyleGAN [9], StyleGAN2 [44], ProjectedGAN [51], DiffGAN [53]). As can be observed, augmenting ADM and DiT backbones with our lightweight graph correction term consistently improves FID and recall over their baseline pointwise counterparts. Notably, these ADM+GFM and DiT+GFM models achieve FID and recall on par with the diffusion and GAN pipelines in Table 15, showing that simply adding GFM as a graph based correction yields significant quality gains, without altering the core architecture or training objective.

G Qualitative Results

Figures 4–8 show additional random samples generated by our models across the five evaluated datasets, providing readers with a broader view of typical generation quality.

Table 14: Sampling cost in terms of number of function evaluations (NFE), average sampling time per sample (in seconds), FID (True→Flow) scores, and recall values for each model on five benchmarks at 256×256 resolution. NFE and timing statistics are computed over 10 independent runs. Our proposed methods (marked with †) incur modest computational overhead but consistently achieve substantially better image quality (lower FID) and diversity (higher recall) across all datasets.

Dataset	Model	NFE (\downarrow)	Time (s) (\downarrow)	FID (\downarrow)	Recall (\uparrow)
LSUN Church	ADM	83.00 ± 7.71	0.61 ± 0.55	7.70	0.39
	ADM+MPNN†	89.00 ± 15.24	1.63 ± 0.28	4.94	0.52
	ADM+GPS†	82.40 ± 13.73	1.38 ± 0.23	4.61	0.51
	DiT	87.80 ± 10.75	1.34 ± 0.16	5.54	0.48
	DiT+MPNN†	100.40 ± 14.25	4.94 ± 0.70	2.92	0.65
	DiT+GPS†	93.80 ± 10.75	2.81 ± 0.32	3.10	0.66
LSUN Bedroom	ADM	91.40 ± 15.05	0.93 ± 0.15	7.05	0.39
	ADM+MPNN†	83.00 ± 14.01	1.76 ± 0.29	4.18	0.54
	ADM+GPS†	77.00 ± 10.82	1.51 ± 0.21	3.97	0.56
	DiT	90.20 ± 20.09	1.38 ± 0.30	4.92	0.44
	DiT+MPNN†	95.60 ± 18.43	2.98 ± 0.57	2.66	0.64
	DiT+GPS†	98.60 ± 24.07	2.96 ± 0.71	3.57	0.65
FFHQ	ADM	83.60 ± 6.68	0.85 ± 0.07	8.07	0.40
	ADM+MPNN†	69.20 ± 8.82	1.34 ± 0.17	5.90	0.62
	ADM+GPS†	79.40 ± 10.55	1.55 ± 0.20	5.09	0.62
	DiT	89.00 ± 8.16	1.36 ± 0.12	4.55	0.48
	DiT+MPNN†	91.40 ± 10.88	2.82 ± 0.33	4.52	0.66
	DiT+GPS†	87.80 ± 11.40	2.62 ± 0.34	4.48	0.65
AFHQ-Cat	ADM	81.80 ± 8.07	0.60 ± 0.06	7.34	0.32
	ADM+MPNN†	83.60 ± 5.50	1.51 ± 0.10	6.97	0.35
	ADM+GPS†	126.80 ± 13.89	2.15 ± 0.23	4.63	0.54
	DiT	77.60 ± 5.50	1.18 ± 0.08	9.05	0.42
	DiT+MPNN†	78.20 ± 8.92	2.45 ± 0.28	8.07	0.51
	DiT+GPS†	84.20 ± 11.71	2.50 ± 0.34	8.98	0.42
CelebA-HQ	ADM	84.20 ± 10.75	0.61 ± 0.08	6.80	0.50
	ADM+MPNN†	82.40 ± 9.37	1.46 ± 0.16	6.28	0.56
	ADM+GPS†	78.80 ± 5.88	1.34 ± 0.10	6.71	0.52
	DiT	91.40 ± 12.13	1.39 ± 0.18	6.23	0.55
	DiT+MPNN†	85.40 ± 7.80	2.62 ± 0.24	6.16	0.57
	DiT+GPS†	81.20 ± 7.00	2.44 ± 0.21	6.18	0.59

Table 15: Performance comparison against a range of leading generative models and the corresponding v_{react} -only baselines on LSUN Church, FFHQ, and LSUN Bedroom at 256×256 resolution. We report total parameters, diffusion-term ($v_{\text{diff-net}}$) parameters, FID (lower is better), and recall (higher is better). Baseline parameter counts were measured from the [6] checkpoints on our hardware; our results are highlighted in light blue. Corresponding $FID(\text{True} \rightarrow \text{VAE})$ values are: LSUN Church = 1.01, FFHQ = 1.05, LSUN Bedroom = 0.64.

Dataset/Model	Total Parameters (M)	$v_{\text{diff-net}}$ (M)	FID (\downarrow) VAE \rightarrow Flow	FID (\downarrow) True \rightarrow Flow	Recall (\uparrow)
LSUN Church					
ADM [6] (Baseline)	356.38	0	-	7.70	0.39
ADM+MPNN(Ours)	379.81	23.43	5.06	4.94	0.52
ADM+GPS (Ours)	374.20	18.13	4.67	4.61	0.51
DiT [6] (Baseline)	456.80	0	-	5.54	0.48
DiT+MPNN (Ours)	502.09	45.29	2.90	2.92	0.65
DiT+GPS (Ours)	481.25	24.45	2.89	3.10	0.66
FM [1]	-	0	-	10.54	-
LDM [5]	-	0	-	4.02	0.52
WaveDiff [41]	-	0	-	5.06	0.40
DDPM [17]	-	0	-	7.89	-
ImageBART [50]	-	0	-	7.32	-
StyleGAN [9]	-	0	-	4.21	-
StyleGAN2 [44]	-	0	-	3.86	0.36
ProjectedGAN [51]	-	0	-	1.59	0.44
FFHQ					
ADM [6] (Baseline)	406.40	0	-	8.07	0.40
ADM+MPNN (Ours)	429.82	23.43	5.61	5.90	0.62
ADM+GPS (Ours)	424.53	18.13	4.80	5.09	0.62
DiT [6] (Baseline)	456.80	0	-	4.55	0.48
DiT+MPNN (Ours)	480.23	23.43	3.80	4.52	0.66
DiT+GPS (Ours)	481.25	24.45	3.95	4.48	0.65
LDM [5]	-	0	-	4.98	0.50
ImageBART [50]	-	0	-	9.57	-
ProjectedGAN [51]	-	0	-	3.08	0.46
StyleGAN [9]	-	0	-	4.16	0.46
LSUN Bedroom					
ADM [6] (Baseline)	406.40	0	-	7.05	0.39
ADM+MPNN (Ours)	429.82	23.43	4.51	4.18	0.54
ADM+GPS (Ours)	424.53	18.13	4.26	3.97	0.56
DiT [6] (Baseline)	456.80	0	-	4.92	0.44
DiT+MPNN (Ours)	480.23	23.43	2.55	2.66	0.64
DiT+GPS (Ours)	481.25	24.45	3.31	3.57	0.65
LDM [5]	-	0	-	2.95	0.48
DDPM [17]	-	0	-	4.90	-
ImageBART [50]	-	0	-	5.51	-
ADM [36]	-	0	-	1.90	0.51
PGGAN [52]	-	0	-	8.34	-
StyleGAN [9]	-	0	-	2.35	0.48
ProjectedGAN[51]	-	0	-	1.52	0.34
DiffGAN [53]	-	0	-	1.43	0.58



Figure 4: Randomly generated samples of LSUN Church using DiT-L/2+MPNN

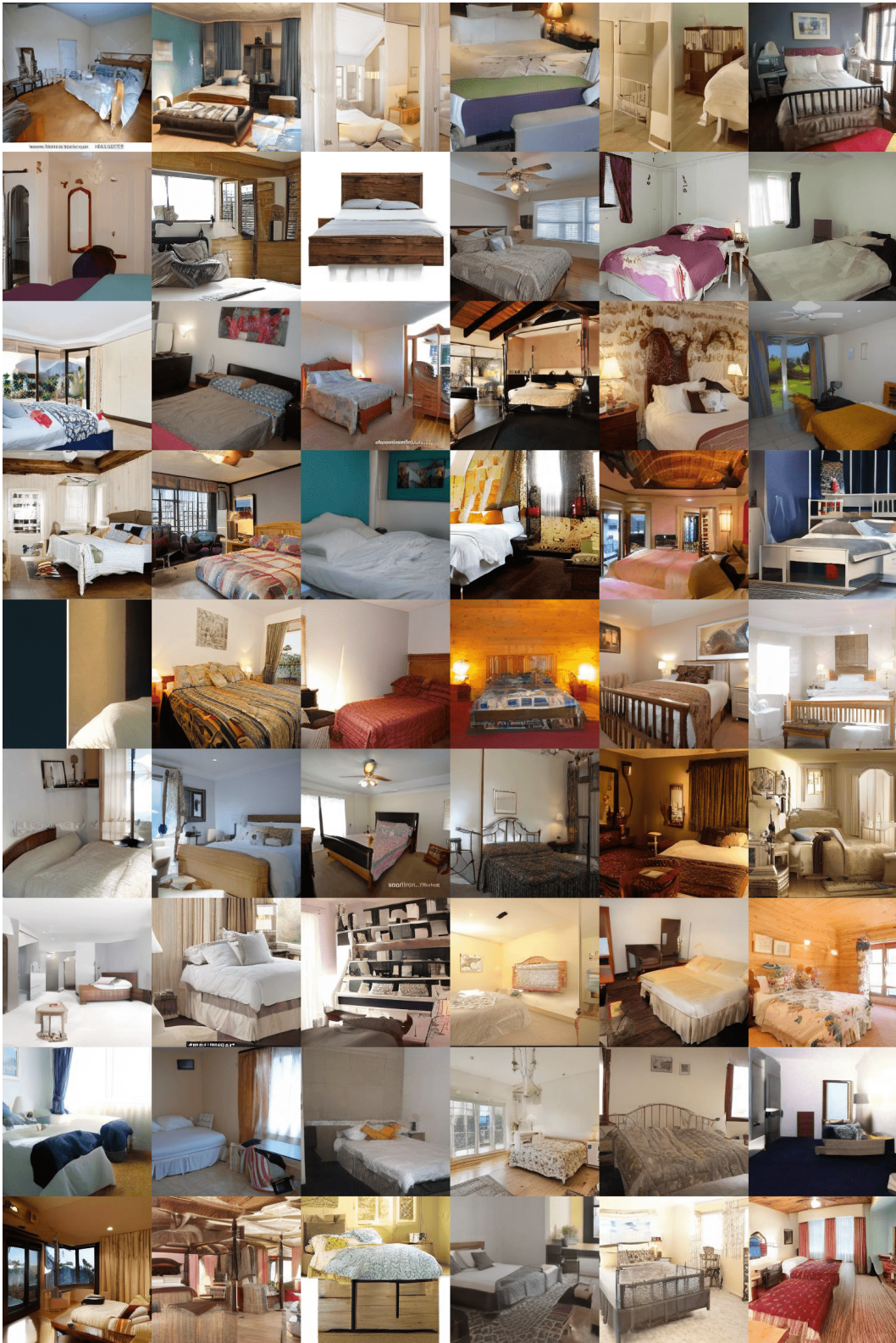


Figure 5: Randomly generated samples of LSUN Bedroom using DiT-L/2+MPNN



Figure 6: Randomly generated samples of FFHQ using DiT-L/2+GPS



Figure 7: Randomly generated samples of CelebA-HQ using DiT-L/2+MPNN



Figure 8: Randomly generated samples of AFHQ-Cat using ADM+GPS